Characterization and analysis of thermoelectric transport in *n*-type $Ba_8Ga_{16-x}Ge_{30+x}$

Andrew F. May,[1,*] Eric S. Toberer,[2] Ali Saramat,[2] and G. Jeffrey Snyder[2]
[1]*Chemical Engineering, California Institute of Technology, 1200 E. California Boulevard, Pasadena, California 91125, USA*
[2]*Materials Science, California Institute of Technology, 1200 E. California Boulevard, Pasadena, California 91125, USA*
(Received 27 May 2009; revised manuscript received 17 August 2009; published 18 September 2009)

The thermoelectric transport properties of polycrystalline, *n*-type $Ba_8Ga_{16-x}Ge_{30+x}$ were characterized from 300 to 1000 K. The carrier density was found to vary precisely with the experimental x as expected from simple electron counting. The experimental data are analyzed within the framework of a single parabolic band model, which is found to accurately describe transport for the compositions of interest for thermoelectric application. The lattice thermal conductivity, calculated with a degeneracy adjusted Lorenz number, does not show a trend with composition and a value of $\sim 1\ \mathrm{Wm^{-1}\,K^{-1}}$ is observed at 300 K. A maximum figure of merit $zT=0.86$ is obtained at 950 K, and the optimal doping level for thermoelectric application is predicted to be $\sim 2\times 10^{20}\ \mathrm{cm^{-3}}$, which corresponds to $Ba_8Ga_{15.75}Ge_{30.25}$ by electron counting. An unexpected transition event is observed near 650 K, which results in a significant increase in the heat capacity.

DOI: 10.1103/PhysRevB.80.125205 PACS number(s): 73.50.Lw, 72.20.Pa, 74.25.Fy, 84.60.Rb

I. INTRODUCTION

The clathrate structure types contain three-dimensional frameworks with voids (cages) where guest atoms (fillers) can reside. The $Ba_8Ga_{16-x}Ge_{30+x}$ compound discussed here has the type I clathrate structure (cubic, space group $Pm\bar{3}n$, No. 223),[1] which possesses two types of cages formed by the Ga-Ge framework and the Ba atoms reside within these cages. The composition $Ba_8Ga_{16}Ge_{30}$ is valence balanced, as each Ba donates two electrons and every Ga utilizes one of these electrons for bonding within the framework. Deviation from this stoichiometry results in doped semiconductor behavior, with excess Ge ($x>0$) giving *n*-type samples and excess Ga ($x<0$) resulting in *p*-type samples.[2–6]

At high temperature, the clathrates have shown to possess thermoelectric efficiency equivalent to state of the art materials such as PbTe and SiGe.[7–9] The thermoelectric efficiency of a material is governed by the figure of merit, $zT=\alpha^2 T/\rho\kappa$. Here, α is the Seebeck coefficient, ρ the electrical resistivity, and κ the thermal conductivity, which is generally considered as the sum of the lattice κ_L and electronic κ_e contributions. The clathrates possess $zT\sim 1$ near 900 K due to the combination of relatively low κ_L and large $\mu m^{*3/2}$, where μ is the mobility and m^* is the effective mass. Thermoelectric efficiency generally optimizes as a function of carrier concentration n with the optimum n typically between 10^{19} and $10^{21}\ \mathrm{cm^{-3}}$.[10] This optimization is primarily associated with the electronic properties, which are often examined via the quantity α^2/ρ (thermoelectric power factor). However, the influence of κ_e must also be taken into account and zT typically optimizes at smaller n than required to optimize α^2/ρ.

A large number of investigations on the low-temperature thermal conductivity of clathrates have been performed.[11–19] The main purpose of these studies is to reveal the role of the filler atom, with filler atom-phonon and filler atom-framework interactions of primary interest. Many clathrates have glasslike thermal conductivity, and similar behavior has been observed in *p*-type $Ba_8Ga_{16-x}Ge_{30+x}$. Interestingly, *n*-type $Ba_8Ga_{16-x}Ge_{30+x}$ has crystalline-like thermal conductivity.[14,16,17]

While many studies continue to investigate the influence of chemical manipulation on the thermoelectric properties of $Ba_8Ga_{16-x}Ge_{30+x}$ (for instance the substitution of Yb for Ba, or In for Ge),[20–23] the transport features inherent to $Ba_8Ga_{16-x}Ge_{30+x}$ have not been completely characterized and analyzed for the compositions of interest to thermoelectric application ($0\leq x\leq 1$ for *n*-type). The objective of this article is to provide a thorough study of the high-temperature transport in polycrystalline, *n*-type $Ba_8Ga_{16-x}Ge_{30+x}$. To complete this task, quantitative agreement between the Hall carrier density and the carrier density expected from electron counting is demonstrated, and the corresponding changes in transport properties are analyzed using classic solutions to the Boltzmann transport equations. The dependence of α, m^*, μ, and κ_L on doping level is addressed and a rigid band model is utilized to estimate the optimum doping level for thermoelectric application.

II. METHODS

A. Synthesis

Polycrystalline $Ba_8Ga_{16-x}Ge_{30+x}$ was prepared by direct reaction of the elements in pyrolitic boron nitride crucibles sealed within evacuated (2×10^{-5} torr) quartz ampoules. High-purity Ga (99.99% metals basis, Aldrich), Ge (99.9999% metals basis, Alfa Aesar), and Ba (distilled, dendritic 99+% metals basis, Aldrich) were utilized, and a slight excess of Ba was employed to account for possible oxidation—nominal compositions were $Ba_{8.2}Ga_xGe_{46-x}$.[24] Mixtures of the elements were heated to 1325 K at 100 K/hr, where the melts were held for 2 hr prior to quenching in air. The resulting ingots were ground under argon in a SPEX SamplePrep 8000 Series Mixer/Mill for a minimum of 1 hr and maximum of 4 hr inside stainless steel vials with stainless steel balls. Fine, homogeneous powders from the high-energy milling were hot pressed in high-density graphite dies (POCO) utilizing roughly 1.1 metric tons of force over a 12 mm diameter at 1100 K. Hot pressing took place over 1 hr in an argon atmosphere, and was followed by 1 hr of stress-free anneal under vacuum.

 ©2009 The American Physical Society

B. Characterization

1. Chemical

Phase purity was investigated using a Phillips X'Pert diffractometer and a LEO 1550 VP scanning electron microscope (SEM). Diffraction data were obtained via Cu K_α radiation and microscopy was performed using both secondary and backscattered electron imaging. During SEM operation, a voltage of 20 kV was utilized and energy dispersive spectroscopy (EDS) was performed to analyze elemental composition. Wavelength dispersive spectroscopy (WDS) was also performed to investigate composition; a JEOL JXA-8200 was employed for WDS. The WDS results represent the average of roughly 25 individual points ($\sim 1\ \mu m^3$ each), where each set of 25 was divided into 5 line scans (5 points per line at 5 μm apart) that probed regions of the sample separated by $\sim 100\ \mu$m. During WDS, an electric potential of 15 kV is utilized and a ZAF correction is employed to account for atomic number, absorption and fluorescence effects. Elemental Ge, GaAs, and benitoite ($BaTiSi_3O_9$) were utilized for the Ge, Ga, and Ba standards, respectively.

2. Transport properties

Electrical transport was characterized via Hall effect, electrical resistivity, and Seebeck coefficient measurements. The Hall coefficient and electrical resistivity were obtained using the van der Pauw method with a maximum current of 10 mA. Hall coefficients (R_H) were measured on two separate systems: a magnetic field of ~ 1 T was utilized for high-temperature measurements while roughly 2 T was employed at room temperature. The absolute Seebeck coefficient (α) was obtained at room temperature using Cu/constantan thermocouples and by accounting for the Cu voltage. High-temperature α measurements employed W/Nb thermocouples and utilized the differential light pipe method discussed in Ref. 25; a $\Delta T \sim 5$ K was employed for all temperatures. Thermal conductivity (κ) was determined via $\kappa = D_T C_P d$, where D_T is the thermal diffusivity, C_P the heat capacity, and d the geometric density. The value of D_T was obtained via a NETZSCH laser flash analysis (LFA) 457. High-temperature heat capacity data were collected from the LFA 457 as well, by utilizing a pyroceram 9606 standard. A NETZSCH 200 series differential scanning calorimeter (DSC) obtained C_P to roughly 775 K using a sapphire standard and a heating rate of 20 K/min with Pt crucibles and Al_2O_3 liners. Thermal gravimetry (TGA) data were obtained in a NETZSCH TG 209 F3 from 300 to 1025 K at 20 K/min under nitrogen. The DSC and TGA data were collected by Lloyd MacPherson of NETZSCH, and all other measurements were performed at the California Institute of Technology and/or the Jet Propulsion Laboratory.

III. RESULTS AND DISCUSSION

A. Phase purity, composition, and carrier density

The samples discussed in this article are given labels (capital letters *A* through *E*) and specific symbols are utilized to present the data, as shown in Table I. Compositional data obtained via WDS are also provided in Table I. The polycrystalline samples were observed to be homogeneous via scanning electron microscopy and electron probe microanalysis. Samples *A*, *B*, and *D* were single phase via x-ray diffraction, while samples *C* and *E* contained a small amount of elemental Ge (refined to less than 1 wt. %), which is a common impurity in polycrystalline $Ba_8Ga_{16-x}Ge_{30+x}$ samples.[26] Phase purity is demonstrated in Fig. 1, where a diffraction scan for the sample containing the most Ge impurity is shown (sample *E*). The inset in Fig. 1 compares the scan shown in Fig. 1 to a phase pure sample (*A*), and the location of the Ge impurity is marked by an asterisk.

TABLE I. Atomic composition of $Ba_8Ga_{16-x}Ge_{30+x}$ samples assessed via wavelength dispersive spectroscopy

Sample	Symbol	Ba at. % (std dev)	Ga at. % (std dev)	Ge at. % (std dev)
A	△	15.09(0.08)	28.13(0.14)	56.78(0.17)
B	□	15.31(0.08)	28.54(0.21)	56.15(0.23)
C	▽	15.12(0.06)	28.66(0.17)	56.21(0.18)
D	○	15.44(0.16)	29.23(0.14)	55.33(0.18)
E	◇	15.10(0.29)	29.87(0.64)	55.03(0.63)

In Fig. 2, the room-temperature Hall carrier concentrations n_H are plotted versus experimental x values. The experimental x values were obtained from the WDS data assuming no vacancies on the framework: $\frac{30+x}{16-x} = \frac{\text{Ge at. \%}}{\text{Ga at. \%}}$. The experimental values agree well with the theoretical n versus x (solid curve), which is obtained by simple charge counting that reveals x free electrons per formula unit (holes are formed for $x < 0$). Note there is a small difference between the chemical n and n_H due to scattering effects, which are discussed below. The agreement between experiment and theory suggests the Zintl formulism for electron counting is strictly obeyed in n-type $Ba_8Ga_{16-x}Ge_{30+x}$ (for the compositions of interest to thermoelectric applications). We note the same conclusion was drawn from a plot using EDS data,

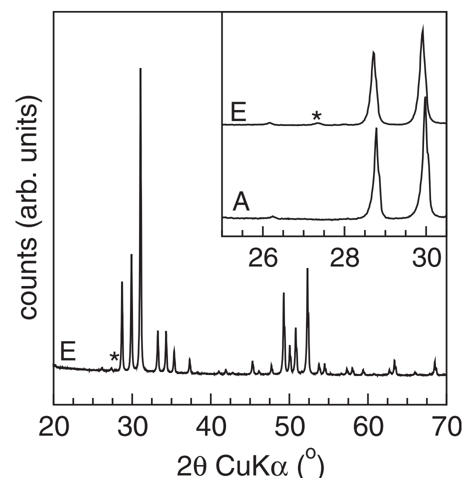

FIG. 1. X-ray diffraction scan of sample *E*, which contains the maximum Ge impurity observed. The inset examines the position around the Ge impurity, the peak of which is marked with an asterisk, and a phase pure sample (*A*) is shown for comparison.

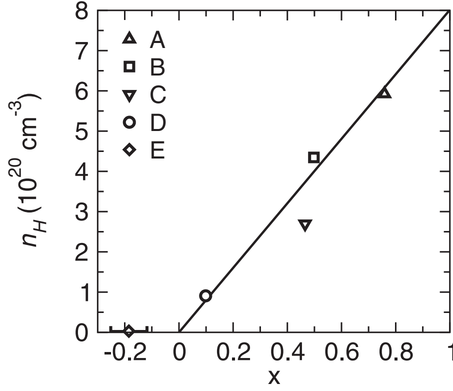

FIG. 2. Room-temperature Hall density as a function of experimental x. The solid line is generated from electron counting assuming $Ba_8Ga_{16-x}Ge_{30+x}$ stoichiometry.

which possesses the same slope as the electron counting line in Fig. 2, but was shifted to excess Ge by roughly $x=0.4$. The use of standards during WDS measurements yields higher accuracy than in EDS measurements and thus the EDS data are omitted for clarity. The atomic percent Ba obtained from WDS reveals greater Ba content than allowed by the crystal structure (8/54=14.8 at. %); this assumes no framework vacancies. The error in Ba content may be related to the use of an oxide for the Ba standard, as similar errors in WDS data were observed for the $La_{3-x}Te_4$ system, where $LaPO_4$ was utilized for the La standard and La content was found to be greater than that allowed by the crystal structure (the same conditions were employed).[27] However, this may also be due to the presence of a barium rich oxide at the grain boundaries, or Ge/Ga vacancies. The error bars shown in Fig. 2 for sample E correspond to the standard error obtained for the mean x values, which were based on roughly 25 point measurements. The error bars for samples A–D are hidden by the size of the data points.

While simple charge counting rules appear to apply assuming no vacancies, the role of vacancies (both framework and filler) remains unclear.[28–30] Ba vacancies have been revealed by refinement of diffraction data,[29] and the literature also contains studies which fit diffraction data to $Ba_8Ga_yGe_z$ where $y+z<46$, as well as $Ba_8Ga_{16-x}Ge_{30+x}$.[30–32] The formation of vacancies in n-type clathrates appears to be most important when compositions lie far from the charge balanced composition.[30,33] Vacancies remove electrons from the system and thus move the Fermi energy (and carrier concentration) towards more reasonable levels (for n-type compositions), as seen in K_8Si_{46-x} and Rb_8Sn_{46-x}.[34]

The growth of single-crystal samples with nominal composition near $Ba_8Ga_{16}Ge_{30}$ frequently results in n-type samples,[7,8] which could be due to greater Ge content than expected. Energetic arguments have been made to suggest $Ba_8Ga_{15}Ge_{31}$ may be more stable than $Ba_8Ga_{16}Ge_{30}$ due to a reduction in Ga-Ga repulsion.[35]

B. Transport properties

1. Electrical transport

The experimental transport data are analyzed using common solutions to the Boltzmann transport equation within the relaxation time approximation. It is assumed that electron conduction occurs within a single parabolic band, which is consistent with prior computational work.[36,37] Also, the equations shown below are valid for a single scattering mechanism where the energy dependence of the carrier relaxation time can be expressed by a simple power law.

TABLE II. Room-temperature properties of $Ba_8Ga_{16-x}Ge_{30+x}$ samples, where the calculated r_H and m^* are obtained assuming acoustic phonon scattering limits μ_H.

Sample	n_H (10^{20} cm^{-3})	r_H	μ_H (cm^2/V/s)	α (μV/K)	m^* (m_e)
A	5.9	1.02	11.6	−52	1.82
B	4.3	1.04	12.8	−65	1.86
C	2.7	1.05	14.4	−81	1.74
D	0.9	1.11	12.1	−159	2.02
E	0.03	1.18	7.2	−143	

The room-temperature Hall data are summarized in Table II, where the corresponding values of the Seebeck coefficient (α) are provided. Hall effect measurements reveal n-type samples, with Hall carrier concentrations between 0.9 and 5.9×10^{20} cm^{-3} for extrinsic samples (samples A–D) at 300 K. The Hall carrier concentration n_H is calculated via $n_H=1/R_He$, where R_H is the Hall coefficient and e the electric charge. The Hall carrier concentration is related to the chemical carrier concentration n via

$$n=r_Hn_H, \tag{1}$$

where the Hall factor r_H is given by

$$r_H=\frac{3}{2}F_{1/2}(\eta)\frac{(1/2+2\lambda)F_{2\lambda-1/2}(\eta)}{(1+\lambda)^2F_\lambda^2(\eta)}, \tag{2}$$

with the Fermi integrals $F_j(\eta)$ defined by

$$F_j(\eta)=\int_0^\infty\frac{\xi^j d\xi}{1+\mathrm{Exp}[\xi-\eta]}. \tag{3}$$

Here, ξ is the reduced carrier energy, η is the reduced electrochemical potential, and λ relates to the energy dependence of the carrier relaxation time, τ, such that $\tau=\tau_0\epsilon^{\lambda-1/2}$ where the expression for τ_0 depends on λ. To determine r_H, values of η must be obtained, which is accomplished via analysis of Seebeck coefficient α data (details below). Note Eqs. (2) and (5) were obtained via integration by parts from the general equations in Ref. 38.

The distinction between n and n_H allows a more self-consistent comparison between experiment and the single band model. The values of n and n_H converge for complete degeneracy ($\eta\gg0$), where $r_H=1$ regardless of the scattering mechanism, as well as for energy-independent carrier relaxation time ($\lambda=0.5$) regardless of the value of η. In a nondegenerate conductor ($\eta\ll0$), r_H equals 1.18 for scattering of carriers via acoustic phonons ($\lambda=0$) and $r_H=1.93$ for scattered by ionized impurities.[38] The values of r_H shown in Table II were generated assuming $\lambda=0$, and r_H for sample E is taken to be the nondegenerate limit. The values of r_H in

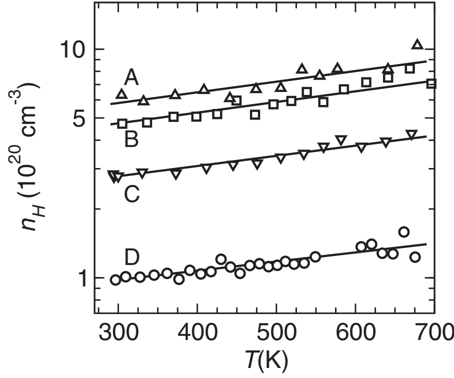

FIG. 3. Temperature dependence of the experimental Hall carrier densities ($n_H = 1/R_He$). The solid lines are provided for visual guidance.

Table II are thus an estimate of the minimum deviation between n and n_H because the introduction of ionized impurity scattering would increase r_H.

In Table II, the data resulting from Hall effect measurements on sample E possess significantly more error than do the data collected on heavily doped samples. This is because sample E is found to behave like an intrinsic semiconductor, and thus the single carrier assumption breaks down. Therefore, the values of n_H and μ_H provided for sample E should not be considered in detail.

The temperature dependence of n_H is shown in Fig. 3. While a slight increase with increasing T is observed, the values of n_H are dominated by extrinsic doping, which is consistent with the electron counting described above. The increase in n_H with T cannot be explained by temperature-dependent r_H when only acoustic phonon scattering is present, in which case r_H increases with increasing T and thus n would increase more rapidly than n_H. A temperature-dependent r_H may explain some, though not all, of the T dependence of n_H if competing scattering mechanisms are present. If ionized impurity scattering is important at low T, the values of r_H would be larger than those shown in Table II, and r_H would decrease with increasing T as acoustic phonon scattering becomes more important.

The Hall mobility μ_H is calculated from the Hall coefficient and electrical resistivity ρ,

$$\mu_H = R_H/\rho. \tag{4}$$

The Hall mobility is related to the drift mobility μ_d by $\mu_H = r_H\mu_d$. Therefore, the theoretical description of μ_H differs slightly from that of μ_d, and the effect is most significant at low n or high T. For a single parabolic band semiconductor, the Hall mobility can be represented by

$$\mu_H = \mu_0 \frac{(1/2 + 2\lambda)F_{2\lambda-1/2}(\eta)}{(1+\lambda)F_\lambda(\eta)}. \tag{5}$$

The value of μ_0 is related to the relaxation time τ_0 by $\mu_0 = e\tau_0/m^*$. When charge carriers are scattered by acoustic phonons ($\lambda=0$ and we define $\mu_0=\mu_{0,L}$), $\mu_{0,L}$ can be calculated from[38]

$$\mu_{0,L} = \frac{e\pi\hbar^4}{\sqrt{2}(kT)^{3/2}} \frac{C_{11}}{E_{def}^2 (m^*)^{5/2}}, \tag{6}$$

where C_{11} is the elastic constant for longitudinal vibrations, E_{def} is the deformation potential, and m^* is the density of states effective mass. In other formulations, μ_0 is defined as the nondegenerate limit of the mobility. This is not the case here, where μ_0 is utilized to relate the experimental μ_H values to basic materials properties. For instance, for $\lambda=0$, the nondegenerate mobility is $\frac{\sqrt{\pi}}{2}\mu_{0,L}$.

The theoretical curves generated for various transport properties are related to the theoretical Hall carrier density via η, λ, m^*, and T:

$$n_H = 4\pi \left(\frac{2m^*kT}{h^2}\right)^{3/2} \frac{F_{1/2}(\eta)}{r_H}. \tag{7}$$

The dependence of μ_H on T and n_H is complex, particularly in materials where multiple scattering mechanisms limit the carrier mean-free path. A proper treatment of μ_H data requires allowance for all relevant scattering mechanisms, including residual resistances associated with grain boundaries and defects. For the current study, we consider the various scattering mechanisms and analyze the data within the limit of what appears to be the dominant scattering mechanism. At moderate temperatures, the mobility of a heavily doped semiconductor is typically limited by acoustic phonon scattering and/or ionized impurity scattering. The effect of ionized impurities is greatest at lower temperatures and acoustic phonon scattering tends to dominate at higher temperatures. Alloy scattering, which has been considered in the $Ba_8Ga_xCu_yGe_{46-x-y}$ system,[39] may also be present and would be most influential at lower temperatures (also modeled with $\lambda=0$). At high temperatures, we expect μ_H to be limited by acoustic phonon scattering, and this assumption ($\lambda=0$) is utilized in the subsequent analysis. The validity of this assumption will be addressed below where the T and n_H dependence of μ_H is considered.

Let us first consider the variation in μ_H with n_H, which is shown in Fig. 4. Figure 4 shows room-temperature data from this study, data reported by Martin *et al.*[26] for 350 K, and theoretical curves based on Eqs. (5)–(7). We note the μ_H values are in agreement with the literature.[3,7] The dependence of μ_H on n_H is found to be in fair agreement with the theoretical description of acoustic scattering. The curves in Fig. 4 were generated using temperature-dependent values of C_{11} from the literature,[40] and a value of $m^*=1.86m_e$, where m_e is the rest mass of an electron. The value of m^* was selected based on similar analysis of the room temperature Seebeck coefficients (see below). The theoretical curves in Fig. 4 were generated using a deformation potential of $E_{def}=8.3$ eV, which is a reasonable value for a doped semiconductor.[38,41] The source of reduced μ_H for sample D is not clear, as this sample was phase pure and demonstrated no other transport irregularities. The effect of residual resistance (via grain boundaries and defects) is to decrease μ_H, although this alone does not appear to explain the deviation from theory for sample D. In the traditional view of ionized impurity scattering, a reduced carrier concentration eventu-

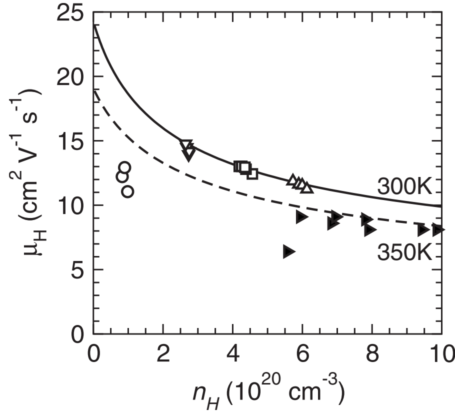

FIG. 4. (a) Room-temperature Hall mobility versus carrier concentration for samples from this study (open markers with symbols as in Table I), as well as data at 350 K from Martin *et al.* (filled markers, Ref. 26). The experimental data are compared to theoretical curves generated assuming the carrier mobility is limited by acoustic phonon scattering (solid curve for 300 K, dashed curve at 350 K).

ally leads to a lower mobility due to decreased screening of the ionized impurities. The suppression of μ_H in sample D may be associated with an additional scattering mechanism, or a processing related feature, and thus no conclusion can be drawn at this time.

As shown in Fig. 5, μ_H decreases with increasing T for samples $A-D$. The temperature dependence of μ_H in a heavily doped semiconductor can usually be modeled by a power law $\mu_H \propto T^{-p}$ when one scattering mechanism limits μ_H for the temperature range of interest. Examining the μ_H data in this manner, we find that the empirically observed parameter p for samples $A-D$ changes with increasing temperature. Such deviations from power law behavior are best observed in a log-log plot, hence the axis selection in Fig. 5. The failure of a single power law to fit the mobility data is likely due to the presence of multiple scattering mechanisms. As can be inferred from Fig. 5, the empirical p is found to increase as the T range of interest increases. This is consistent with competing scattering mechanisms, where the influence of acoustic phonon scattering becomes increasingly important as T rises. We note a single p value describes the data

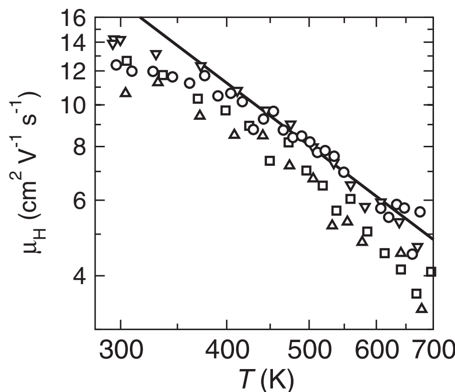

FIG. 5. Hall mobility versus temperature for samples $A-D$ presented in log-log format, with a $T^{-1.5}$ decay shown for comparison.

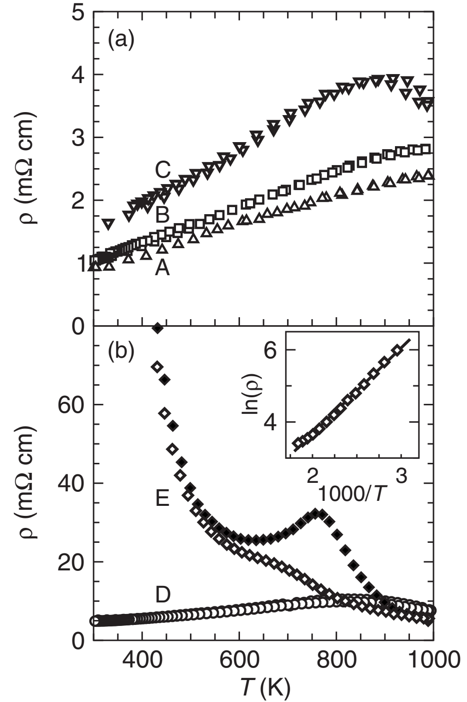

FIG. 6. Electrical resistivity versus temperature for (a) heavily doped ($A-C$) and (b) moderately doped (D) and near-insulating (E) samples. The inset in (b) shows the intrinsic behavior of sample E between 340 and 540 K, where an energy gap of E_g=0.41 eV is obtained from the linear fit shown.

much better if the value of n_H is taken as a constant. From simple electron counting, we do not expect the carrier density to depend on temperature (before band-gap effects are introduced) and thus it is possible that the unexpected temperature dependence of n_H leads to an incorrect $\mu_H(T)$. Interestingly, at high temperatures, $p>1.5$ is observed. The theoretical dependence of μ_H on T for charge carriers scattered by acoustic phonons is more complex than initially observed via Eqs. (5) and (6), and $p>1.5$ can be explained via Eqs. (5) and (6) when C_{11}, m^*, and E_{def} depend on T. Of course, at high T the single carrier description fails and an underestimated μ_H is obtained.

The electrical resistivity increases with decreasing n and increasing temperature for samples $A-D$, as expected for a heavily doped semiconductor [see Fig. 6(a)]. The effect of thermally activated minority carriers can be observed at high temperature as the resistivity begins to decrease for samples C and D. The increase in ρ with increasing T corresponds to the decrease in μ_H shown in Fig. 5(a).

The resistivity of sample E displays the temperature dependence commonly observed for an intrinsic semiconductor. If the decrease in ρ is assumed to be due to the thermal excitation of charge carriers across the energy gap, yielding $\rho \propto \text{Exp}(E_g/2kT)$, a band gap E_g of 0.41 eV is obtained from the fit (solid line) in the inset of Fig. 6(b). The high-temperature behavior of this sample is examined in Fig. 6(b), where an event is observed upon heating. This event is also observed in the Seebeck coefficient (α), where a decrease in the magnitude of α is observed at high temperature (see Fig. 7). The event (increase in ρ) observed in sample E occurred

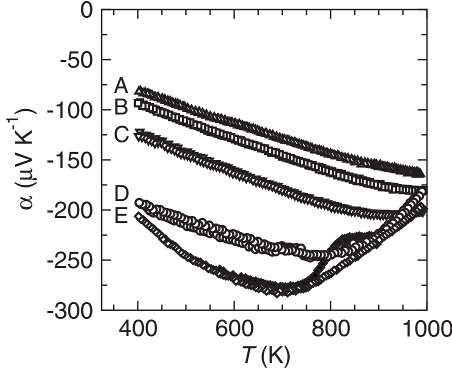

FIG. 7. Seebeck coefficient versus temperature demonstrates behavior expected for heavily doped semiconductors.

during heating upon consecutive cycles for both ρ and α, and was not observed upon cooling. This behavior is not expected and is discussed below.

As shown in Fig. 7, the Seebeck coefficients have the sign and temperature dependence expected for heavily doped, n-type semiconductors. Consistent with the behavior of ρ in Fig. 6(a), the magnitudes of the Seebeck coefficients of the low n samples display maxima at high temperature, where the thermally activated holes reduce the thermoelectric voltage. By utilizing $E_g \sim 2e\alpha_{\max}T_{\max}$,[42] a thermal band gap of $\sim$0.39 eV is observed for samples C, D, and E, which is consistent with E_g estimated from electrical resistivity data for sample E. The values of E_g reported here are consistent with *ab initio* electronic structure calculations reported by Blake *et al.* ($E_g \sim 0.5$ eV),[36] while calculations by Madsen *et al.* predicted a larger value ($E_g \sim 0.9$ eV).[37]

In Fig. 8, the room temperature $|\alpha|$ is plotted versus n_H, and data from this study and the literature are compared to two theoretical calculations. The solid curve is generated using a single parabolic band (SPB) model, the details of which are provided below. The dashed curve in Fig. 8 is the result of *ab initio* calculations previously reported by Madsen *et al.*[37] The experimental data are well described by the SPB

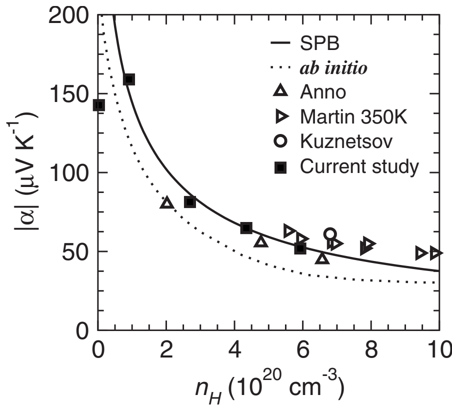

FIG. 8. Absolute value of the room temperature Seebeck coefficients from this study and the literature are compared to a single parabolic band (SPB) model, as well as the *ab initio* calculation by Madsen *et al.* (Ref. 37) Note the data from Martin *et al.* is reported at 350 K. The experimental data shown was taken from References 3, 7, and 26.

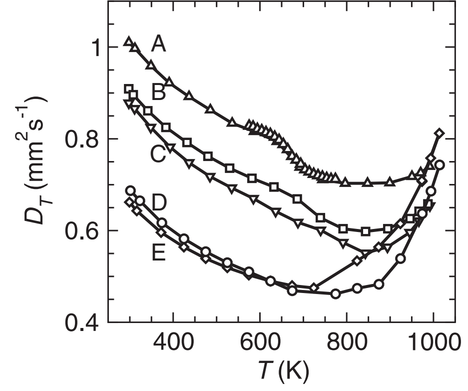

FIG. 9. The thermal diffusivity versus temperature shows the expected temperature dependence at moderate T. Above 650 K, sudden decreases in D_T are observed. This is most readily seen in the data for sample A, where D_T was collected in smaller T intervals to examine this behavior.

model, the curvature of which also agrees well with the *ab initio* results, though a small change in curvature exists at high n. The agreement between theory and experiment strongly justifies the use of a single parabolic band model during the analysis of electronic transport, particularly for the $Ba_8Ga_{16-x}Ge_{30+x}$ compositions of interest for thermoelectric application. We note the *ab initio* results shown here were extracted from the published report, which was originally presented as a function of electrons per formula unit (chemical n), and is thus not a direct comparison with the Hall data and contains minor error associated with data extraction.

The Seebeck coefficient is analyzed within the single parabolic band assumption:

$$\alpha = \frac{k}{e}\left(\frac{(2+\lambda)F_{\lambda+1}(\eta)}{(1+\lambda)F_{\lambda}(\eta)} - \eta\right). \tag{8}$$

The solid curve shown in Fig. 8 is generated by assuming the carrier mobility is limited by acoustic phonon scattering ($\lambda=0$), and an effective mass of $m^*=1.86m_e$ is utilized to calculate n_H via Eq. (7).

2. Thermal transport

The thermal conductivity is calculated via $\kappa = D_T C_P d$, where D_T is the thermal diffusivity, C_P the heat capacity, and d the density. The thermal diffusivity data obtained from laser flash analysis are shown in Fig. 9. The value of D_T is found to decrease with decreasing n and temperature, for $T < 800$ K. An unusual (sudden) decrease in D_T is observed in samples $A-C$, which is most readily observed in sample A near 650 K. Additional D_T data were taken for sample A using 10 K increments, and the event appears to occur continuously. This event is also observed in the heat capacity, as discussed below.

The high-temperature heat-capacity is shown in Fig. 10. The C_P data reported here is consistent with low temperature data from in the literature,[14] an estimate of which is shown as a solid line in Fig. 10 below 300 K. Also, the room-temperature heat capacity is found to be approximately equal

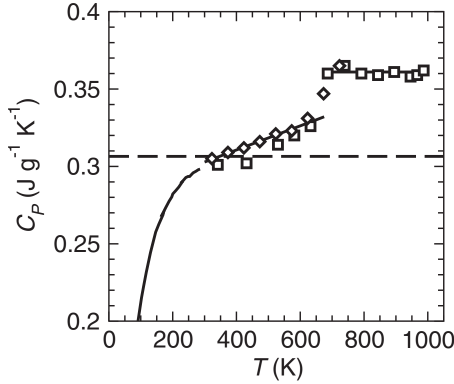

FIG. 10. The measured heat capacity agrees well with previously reported low temperature data, (Ref. 14) and is found to increase linearly until ~650 K at which point an event is observed. Two linear fits are utilized to describe the data, with a constant value of 0.361 J/g/K employed above 675 K. Squares are shown for data taken from the LFA 457 (sample B) and diamonds represent data obtained from the DSC (sample E). The dashed line represents the Dulong-Petit estimation.

to the value obtained using the method of Dulong-Petit (dashed line, 0.3065 J/g/K), and thus the C_P reported is physically reasonable. At moderate T, C_P increases linearly with increasing temperature, presumably due to an increase in the anharmonic and/or electronic contributions. The linear temperature dependence is lost at roughly 650 K, where an event occurs and C_P increases abruptly. Above this event, C_P appears to be independent of temperature, and a value of 0.361 J/g/K is utilized to draw the solid line in Fig. 10 between 675 and 1000 K. These features are not addressed in the literature, and will be briefly discussed below. The linear fit from 300 to 675 K (C_P=7.8×10^{-5}+0.28 in J/g/K) followed by a constant value of 0.361 J/g/K was utilized to calculate κ for all compositions. We note the C_P presented here differs from that in Ref. 9, where no event was observed.

The temperature dependence of $\kappa = D_T C_P d$ is shown in Fig. 11. The decrease in κ with decreasing n and increasing T is expected for a doped crystalline semiconductor. A clear increase in κ associated with the event in C_P is observed near 675 K, which is indicated by the dashed, vertical line in Figs. 11(a) and 11(b). At high temperatures, the thermal excitation of charge carriers leads to an increase in κ via an increased electronic contribution. The electronic component of the thermal conductivity (κ_e) has contributions from electrons, holes, and the bipolar conductivity (κ_b). The effect of κ_b will be addressed below. However, it is only at high temperature that the use of a single band (electrons only) model breaks down. Therefore, the moderate temperature data should be well characterized by assuming only electrons contribute to κ_e.[43]

The lattice contribution to the thermal conductivity is shown in Fig. 11(b), where no trend with compositional is observed. The values of κ_L are calculated from $\kappa_L = \kappa - \kappa_e$, where κ_e is estimated via the Wiedemann-Franz relationship ($\kappa_e = LT/\rho$). The Lorenz number L is calculated by employing a single parabolic band model,

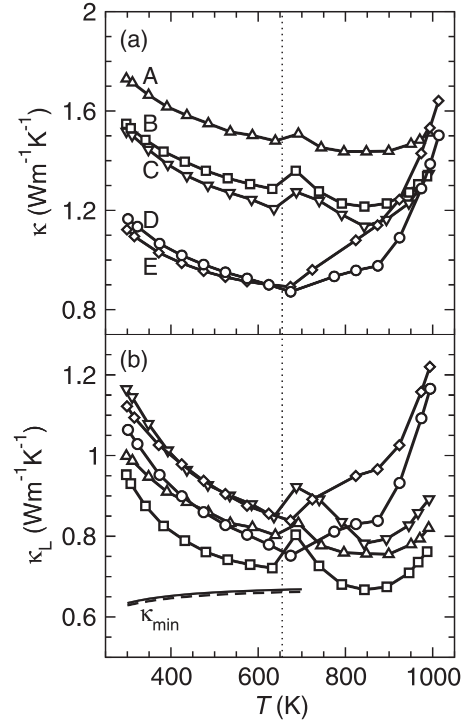

FIG. 11. (a) Total thermal conductivity and (b) lattice thermal conductivity versus temperature. The estimated κ_L values approach the theoretical κ_{min} (solid and dashed curves for samples A and E) before the estimated κ_L begins to increase due to the unaccounted for bipolar contribution at high T. A clear increase in κ associated with the abrupt increase in C_P can be observed (marked by dotted curve).

$$L = \frac{k^2}{e^2} \frac{(1+\lambda)(3+\lambda)F_\lambda(\eta)F_{\lambda+2}(\eta) - (2+\lambda)^2 F_{\lambda+1}(\eta)^2}{(1+\lambda)^2 F_\lambda(\eta)^2}. \tag{9}$$

Here, the carrier mobility is assumed to be limited by acoustic phonon scattering ($\lambda=0$) and the reduced Fermi energy η is obtained as a function of temperature from the experimental Seebeck coefficients using Eq. (8). As stated above, the values of L obtained from this method are most accurate for moderate temperatures where the single band model applies, the region in Fig. 12 where L values are decreasing with increasing T. At higher T, this approximation breaks down and κ_L begins to increase because κ_b is not included in the single band definition of L.

Also shown in Fig. 11(b) are theoretical values of the minimum lattice thermal conductivity, κ_{min}. Consistent with the observed κ_L, the theoretical κ_{min} shows little composition dependence (the calculations are for samples A and E). At moderate temperatures, κ_L approaches κ_{min}. Thus, even though n-type $Ba_8Ga_{16-x}Ge_{30+x}$ demonstrates crystalline-like thermal conductivity, the absolute value of κ_L appears to approach the amorphous limit at high temperatures (in the absence of κ_b). The values of κ_{min} were obtained using Cahill's formulation,[44]

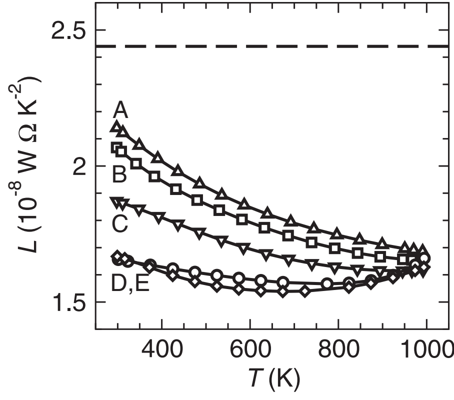

FIG. 12. Lorenz number versus T are significantly lower than the metallic limit, which is represented by the dashed line.

$$\kappa_{\min} = \left(\frac{\pi}{6}\right)^{1/3} k_b V^{-2/3} \sum_i v_i \left(\frac{T}{\Theta_i}\right)^2 \int_0^{\Theta_i/T} \frac{x^3 e^x}{(e^x-1)^2} dx \quad (10)$$

where the summation is over the one longitudinal and two transverse modes, V represents the average volume per atom, $\Theta_i = v_i(\hbar/k_b)(6\pi^2/V)^{1/3}$, and v_i is the sound velocity for the longitudinal and transverse modes (see Table III).

The lattice thermal conductivity decreases with increasing T for moderate temperature, suggesting κ_L decreases due to an increase in phonon-phonon scattering with rising temperature. In a crystalline material, κ_L should decay as T^{-1} when phonon-phonon scattering limits the phonon mean free path (in the temperature range where $C_P \sim$ constant), but κ_L remains finite at high temperatures (hence $\kappa_{\min}$). Thus, for phonon-phonon scattering alone, the physical description of high-temperature thermal transport in a crystalline material is $\kappa_L = \kappa_{\min} + \kappa_0/T$ and the $\kappa_{\min}$ term is important when it is comparable to κ_0/T. The data shown in Fig. 11(b) are well described by such behavior (before the onset of bipolar conduction at high T), and fitting results in $\kappa_{\min} \sim 0.56(0.06)$ $\mathrm{Wm^{-1}\,K^{-1}}$ and $\kappa_0 = 150(30)$ $\mathrm{Wm^{-1}}$ with standard deviations given in parenthesis. Note the good agreement between the value of $\kappa_{\min}$ obtained via this method and that from Eq. (10) (~ 0.66, $\mathrm{Wm^{-1}\,K^{-1}}$). Therefore, the high-temperature κ_L behavior in $Ba_8Ga_{16-x}Ge_{30+x}$ is likely determined by phonon-phonon interactions (assuming the bipolar thermal conductivity is accounted for). The low temperature thermal transport is in agreement with this conclusion, as κ_L of n-type $Ba_8Ga_{16-x}Ge_{30+x}$ increases with decreasing T to roughly 10 K.

It has been shown that the classic definition of the phonon mean-free-path l is inconsistent with phonon lifetimes measured via inelastic neutron scattering.[18] The phonon mean-free paths are generally obtained via $\kappa_L = (1/3) d C_P v_m l$, where the mean sound velocity is given by $v_m = 3^{1/3}(v_l^{-3} + 2v_t^{-3})^{-1/3}$. Indeed, this equation suggests that l is on the order of 6 Å, which would imply the phonon lifetimes are a fraction of a picosecond (~ 0.2 ps). In the case of thermal transport via acoustic phonons, as in κ_L for the $Ba_8Ga_{16-x}Ge_{30+x}$ system, perhaps a more appropriate mean-free path to consider is that of the acoustic phonons, as these carry most of the heat. In this case, the appropriate definition is $\kappa_L = (1/3) d C_{ac} v_m l_{ac}$, where l_{ac} is the mean-free path of acoustic phonons and the volumetric specific heat of acoustic phonons is $dC_{ac} = dC_P/n_a$, where n_a is the number of atoms per primitive cell and d is again density. Using this equation, and the data shown in Table III, it appears that the low κ_L in $Ba_8Ga_{16-x}Ge_{30+x}$ is largely a result of the suppression of the volumetric specific heat of acoustic phonons due to the large unit cell. This formulism leads to $l_{ac} \sim 300$ Å, which corresponds to phonon lifetimes near 10 ps, which are larger than those obtained via neutron scattering (~ 2 ps). Clearly, as discussed in Ref. 18, the microscopic representation of the kinetic theory is likely required.

At high temperature, κ_L appears to increase, but this is an artifact of the above analysis because the bipolar thermal conductivity (κ_b) is not included. The bipolar thermal conductivity arises when both holes and electrons are present and contributing to the electrical conductivity, and is largest when the conductivity of minority and majority carriers is equal. The common expression for κ_b is

$$\kappa_b = \frac{\sigma_h \sigma_e}{\sigma}(\alpha_h - \alpha_e)^2 T, \quad (11)$$

where α_e and α_h are the Seebeck coefficients of electrons and holes, respectively, and σ is the sum of the electron conductivity (σ_e) and hole conductivity (σ_h). In the intrinsic regime, the quantity ($\alpha_h - \alpha_e$) is proportional to E_g/kT and thus κ_b can be large.[45] In Fig. 11, the increase in κ is observed to be most significant for samples with lower n_H. This is in agreement with the basic theory for κ_b and thus we believe κ_b is the primary source for increased κ at high T, as opposed to a contribution from optical phonons.

Alternatively, κ_L can be estimated from a plot of κ versus $1/\rho$ for various samples at a particular temperature. This method assumes $\kappa = \kappa_L + LT/\rho$. Performing this task yields $\kappa_L = 1.1$ $\mathrm{Wm^{-1}\,K^{-1}}$ and $L = 1.78 \times 10^{-8}$ $\mathrm{W\Omega\,K^{-2}}$ at 300 K, and the change with increasing temperature occurs as expected: at 500 K this approach yields $\kappa_L = 0.88$ $\mathrm{Wm^{-1}\,K^{-1}}$ and $L = 1.73 \times 10^{-8}$ $\mathrm{W\Omega\,K^{-2}}$.

In Table III, speed of sound corresponding to the longitudinal (v_L) and transverse (v_t) modes are provided for samples A and E. The similarity in v_L for the two different samples suggests the elastic constant C_{11} does not vary much with composition, and thus composition dependent C_{11} cannot explain the lower than expected μ_H in sample D. Also shown in Table III are experimental and theoretical values for κ_L, as well as the calculated Debye temperatures (Θ_D) and Grüneisen parameters (γ) for these samples (at 300 K, calculated using equations in Ref. 46). The theoretical κ_L is calculated

TABLE III. Room-temperature ultrasonic data and calculated properties of $Ba_8Ga_{16-x}Ge_{30+x}$ samples.

Sample	v_L m/s	v_t m/s	v_m m/s	$\kappa_{L,\mathrm{exp}}$ W/m/K	$\kappa_{L,\mathrm{theory}}$ W/m/K	Θ_D K	γ –
A	4500	2690	2970	1.0	2.1	311	1.62
E	4510	2630	2920	1.1	1.9	306	1.55

utilizing Slack's formulation,[46] which predicts κ_L at Θ_D to be

$$\kappa_L = \frac{H\bar{M}V^{1/3}\Theta_D^2}{n_a^{2/3}\gamma^2}, \tag{12}$$

where γ is the Grüneisen parameter, $\bar{M}$ the average atomic mass, $n_a=54$ is the number of atoms per primitive cell, and the constant $H=3.18$ and 3.16×10^7 s^{-3} K^{-3} for samples A and E, respectively (H is function of γ).[46] The agreement between experimental and theoretical κ_L is reasonable for such a simple theory, which only considers thermal resistance from Umklapp processes. To calculate the Grüneisen parameter,[46] a thermal expansion coefficient of 1.5×10^{-5} K^{-1} is selected, which is an average of the reported values.[9,40] Note the Debye temperatures in Table III are consistent with those in the literature.[14,18]

As shown in Fig. 12, the Lorenz numbers utilized to determine κ_L are significantly smaller than the metallic limit of 2.44×10^{-8} WΩ K^{-2}, which is shown as the dashed line in Fig. 12. As expected, the calculated L values decrease with increasing temperature (due to decreasing η), and at high-temperatures L rises due to the failure of a single band model. The simplest analysis for κ_e utilizes the metallic limit for L, which commonly overestimates the electronic contribution and leads to reduced κ_L. For example, at ~800 K the value of κ_L for sample A is ~0.49 W/m/K using the metallic limit of L and ~0.76 W/m/K using $L\sim1.75\times10^{-8}$ WΩ K^{-2} (obtained from single band analysis). Of course, there are cases where L is greater than the metallic limit, but this generally occurs when the carrier mobility is limited by ionized impurity scattering. Therefore, the literature values for κ_L are often underestimated, which can lead to improper conclusions regarding appropriate methods for further optimization of thermoelectric efficiency.

C. Thermoelectric efficiency

The thermoelectric figure of merit zT is shown as a function of temperature in Fig. 13. The values of zT are calculated using polynomial fits to the α,ρ, and D_T data presented, as well as the two-part fit shown in Fig. 10 for C_P. As shown in Fig. 13, the maximum value of zT is found to be ~0.86 at 950 K, and occurs in samples with $n=2.7$ and 4.4×10^{20} cm^{-3} at 300 K (C and B, respectively). Samples with lower doping levels (D,E) display smaller zT due to higher ρ, and possess a maximum zT at lower T. This temperature dependence is expected because samples with a lower n_H possess a greater compensation (reduction by minority carriers) of the Seebeck coefficient and a larger increase in κ due to κ_b (for a given T). Sample A, which has the largest n_H at 300 K, displays a lower value of zT for all T, likely due to the lower value of $|\alpha|$. We note that we have previously observed permanent changes in the material properties of n-type $Ba_8Ga_{16-x}Ge_{30+x}$ for characterization to 1050 K,[24] and thus thermoelectric operation above 1000 K is unlikely. The optimum n_H values are found to be consistent with the simple theory outlined by Ioffe,[10] which predicts an optimum carrier density near 4×10^{20} cm^{-3} for n-type $Ba_8Ga_{16-x}Ge_{30+x}$ operation at 950 K (based on room-temperature m^*).

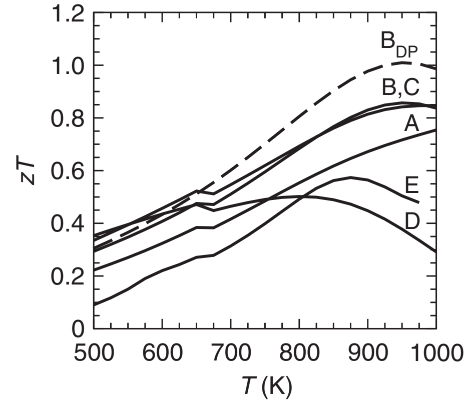

FIG. 13. The temperature dependent zT reveal a maximum near 950 K for samples B and C. The value of zT obtained using the Dulong-Petit estimate of C_P is provided by the curve labeled B_{DP}. For sample E, fits to the cooling data for α and ρ were utilized to generate zT, for all other samples both heating and cooling were utilized to obtain zT.

Also shown in Fig. 13 is the zT curve generated for sample B (B_{DP}) using the Dulong-Petit heat capacity ($C_P=0.3065$ J/g/K). This calculation reveals that zT reaches unity at 950 K for the common C_P assumption. This curve can be used to provide a direct comparison with literature data utilizing C_P=0.3065 J/g/K. Note the zT values presented here do not account for thermal expansion effects. It has been shown that including the effects of thermal expansion in ρ and D_T will lead to a ~3% reduction in zT for $Ba_8Ga_{16-x}Ge_{30+x}$.[9] The zT values shown here are consistent with those presented for polycrystalline samples,[9,26] and are lower than those reported by Saramat *et al.* for single crystal samples ($zT\sim1.3$ at 935 K).[8] While the C_P utilized by Saramat *et al.* is lower than that utilized here, this effect alone does not explain the observed discrepancy and thus the larger zT may be related to increased mobility in single crystals.

The carrier concentration dependence of zT is well described by conventional theory, as shown in Fig. 14. In Fig. 14, the experimental zT at 600 K is plotted versus n_H (at 600 K) and is compared to single parabolic band models, the details of which are described below. The experimental data are well described by the rigid band models, which show a maximum zT of 0.5 near 2×10^{20} cm^{-3} (at 600 K). This electron count corresponds to roughly $Ba_8Ga_{15.75}Ge_{30.25}$.

The predicted carrier dependence is believed to be accurate because the Seebeck coefficients are well described by a single band model (Fig. 8) and the value of κ_L did not demonstrate any trend with composition [Fig. 11(b)]. Also, the data presented in Fig. 14 is for ~600 K, where the single carrier description should be valid. It is possible the theoretical curves underestimate zT at high n_H ($>8\times10^{20}$ cm^{-3}), as the *ab initio* Seebeck coefficient curve in Fig. 8 has less n dependence than expected from the single-band description. We note that the theoretical curves are plotted as a function of n_H at 600 K, and thus a shift to lower room temperature n_H is expected. However the samples are extrinsically doped and n_H varies only slightly with temperature [Fig. 5(b)]. The optimum doping level estimated in Fig. 14 is likely applicable to high temperatures, although the effect of minority carriers must be considered.

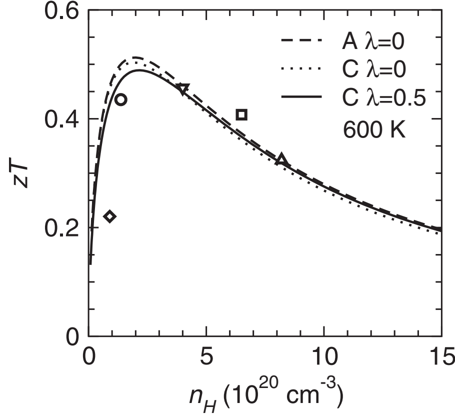

FIG. 14. The experimental zT is plotted versus n_H with all parameters obtained at 600 K. Also shown are three single band models, which demonstrate the expected dependence of zT on n_H at 600 K. The curves with $\lambda=0$ are generated assuming acoustic phonon scattering limits the carrier mobility, and $\lambda=0.5$ implies an energy independent mobility. The input parameters for these curves are given in Table IV.

The theoretical curves in Fig. 14 are calculated using

$$zT = \frac{\alpha^2}{L + (\psi\beta)^{-1}}, \tag{13}$$

where

$$\beta = \frac{\mu_0 (m^*/m_e)^{3/2} T^{5/2}}{\kappa_L} \tag{14}$$

and

$$\psi = \frac{8\pi e}{3}\left(\frac{2m_e k}{h^2}\right)^{3/2}(1+\lambda)F_\lambda(\eta). \tag{15}$$

The values of μ_0, m^*, and κ_L are obtained at the temperature of interest, and are consistent with the type of carrier scattering assumed (λ). The values of α, and L are calculated using Eqs. (8) and (9), and as in Figs. 4 and 8 the corresponding carrier density is calculated using Eq. (7). The zT expression is developed using the drift mobility, $\mu_d=\mu_H/r_H$, and the value of μ_0 is obtained from Eq. (5) using experimental μ_H. For $\lambda=0$, $\mu_0>\mu_H$ while for $\lambda=0.5$ $\mu_0=\mu_H$. The μ_0 term is strictly associated with the thermal (or lattice) mobility, and thus an increase in μ_0 may be observed in single crystal samples. All of the necessary expressions can be found in Ref. 38.

Consistent with rigid band conduction, similar optimum doping level and maximum zT are obtained regardless of which data sets (which sample) are utilized to generate the input parameters. The selection of dominant scattering mechanism (within reason) also has little impact on the optimum doping level and maximum zT. When energy independent scattering is assumed ($\lambda=0.5$), the theoretical zT is very similar to that obtained from the assumption of acoustic phonon scattering, as observed by the similarity between the solid and dotted black curves.

TABLE IV. Parameters for theoretical zT versus n_H at 600 K

Sample	λ	μ_0 (cm^2/V/s)	m^* (m_e)	κ_L W/m/K
A	0	7.6	2.7	0.81
C	0	8.3	2.7	0.87
C	0.5	5.9	1.8	0.80

Perhaps the simplest way to enhance zT in this system is to reduce κ_L via alloying. In fact, substituting Yb on the Ba site has shown to reduce κ_L,[22] although the carrier density was found to increase with increasing Yb content suggesting the framework composition was not fixed. The theoretical zT for a given κ_L is easily calculated within the model presented here, and given the agreement between theory and experiment we expect the values obtained to be fairly accurate. Assuming a 20% decrease in κ_L at 600 K, and using the input parameters for sample *A* from Table IV, a maximum zT of 0.61 is obtained. This corresponds to a minor reduction (8%) in optimum doping level, as expected for a simple semiconductor.[10,47] It therefore seems reasonable that the zT of a polycrystalline *n*-type $Ba_8Ga_{16-x}Ge_{30+x}$ based compound could exceed unity at high temperatures.

D. Transition event

A transition event is observed in the heat capacity (Fig. 10) and corresponding thermal diffusivity (Fig. 9) of heavily doped samples near 675 K, as well as in the Seebeck coefficient and electrical resistivity (Figs. 6 and 7) of the intrinsic sample at higher temperatures. The transition is most pronounced in C_P versus T, where a sharp increase is followed by a plateau, which is observed on heating and cooling. This behavior results in the increase in κ near 675 K. Similar behavior can be observed in the κ data presented by Saramat *et al.* for single crystals, and this feature was confirmed to be correlated to an increase in C_P. The polycrystalline samples reported in Ref. 26 also displayed an event in the heat capacity, which looks very similar to the data presented here.[48] We note no weight loss was observed by thermogravimetric analysis up to 1025 K.

First attempts to isolate the origin of this transition event have been unsuccessful. High-temperature laboratory x-ray diffraction revealed a linear increase in lattice parameter with increasing temperature, and no clear trends were observed in the thermal displacement parameters. Thermal expansion data presented by Okamoto *et al.* also shows a relatively smooth thermal expansion in $Ba_8Ga_{16}Ge_{30}$ through 900 K, as well as a linear temperature dependence of the elastic constants.[40] It remains unclear if these events are intrinsic to $Ba_8Ga_{16-x}Ge_{30+x}$, and further work needs to be performed to isolate the origin of this event.

IV. CONCLUSION

The dependence of carrier concentration on composition in *n*-type $Ba_8Ga_{16-x}Ge_{30+x}$ samples agrees very well with the theoretical carrier density obtained from simple electron

counting. The transport properties vary as expected with doping level and temperature, and a maximum zT of $\sim$0.86 is obtained at 950 K. The lattice thermal conductivity is found to be limited by phonon-phonon interaction, and a value of roughly 1 W/m/K is observed at 300 K (no trend with composition is observed). The data are well described by a single parabolic band model, which predicts an optimum doping level near 2×10^{20} cm^{-3} ($Ba_8Ga_{15.75}Ge_{30.25}$) at 600 K. An event is observed in electrical and thermal data, which results in a sudden increase in C_P and a sudden decrease in D_T. The origins of this transition are unclear, and it is possible the event is related to an impurity, thus further investigation is required.

ACKNOWLEDGMENTS

The Jet Propulsion Laboratory, Beckman Foundation, and the Swedish Bengt Lundqvist Minne Foundation are gratefully acknowledged for support. We thank L. MacPherson of NETZSCH for carefully performing TGA and DSC measurements, T. Ikeda for obtaining WDS data, and L. D. Zoltan for Seebeck coefficient measurements. Finally, we thank G. S. Nolas for discussions regarding the event in C_P.

*may@caltech.edu

[1] B. Eisenmann, H. Schaefer, and R. Zagler, J. Less Common Met. **118**, 43 (1986).
[2] H. Anno, M. Hokazono, M. Kawamura, J. Nagao, and K. Matsubara, Proceedings of the Twenty First International Conference on Thermoelectrics 2002 (unpublished) pp. 77–80.
[3] H. Anno, M. Hokazono, M. Kawamura, and K. Matsubara, Proceedings of the Twenty Second International Conference on Thermoelectrics 2003 (unpublished) pp. 121–126.
[4] M. A. Avila, K. Suekuni, K. Umeo, and T. Takabatake, Physica B **383**, 124 (2006).
[5] V. Pacheco, A. Bentien, W. Carrillo-Cabrera, S. Paschen, F. Steglich, and Yu. Grin, Phys. Rev. B **71**, 165205 (2005).
[6] A. Bentien, V. Pacheco, S. Paschen, Yu. Grin, and F. Steglich, Phys. Rev. B **71**, 165206 (2005).
[7] V. L. Kuznetsov, L. A. Kuznetsova, A. E. Kaliazin, and D. M. Rowe, J. Appl. Phys. **87**, 7871 (2000).
[8] A. Saramat, G. Svensson, A. E. C. Palmqvist, C. Stiewe, E. Mueller, D. Platzek, S. G. K. Williams, D. M. Rowe, J. D. Bryan, and G. D. Stucky, J. Appl. Phys. **99**, 023708 (2006).
[9] E. S. Toberer, M. Christensen, B. B. Iversen, and G. J. Snyder, Phys. Rev. B **77**, 075203 (2008).
[10] A. F. Ioffe, *Semiconductor Thermoelements and Thermoelectric Cooling* (Infosearch Ltd, London, 1957).
[11] G. S. Nolas, J. L. Cohn, G. A. Slack, and S. B. Schujman, Appl. Phys. Lett. **73**, 178 (1998).
[12] J. L. Cohn, G. S. Nolas, V. Fessatidis, T. H. Metcalf, and G. A. Slack, Phys. Rev. Lett. **82**, 779 (1999).
[13] G. S. Nolas, T. J. R. Weakley, J. L. Cohn, and R. Sharma, Phys. Rev. B **61**, 3845 (2000).
[14] B. C. Sales, B. C. Chakoumakos, R. Jin, J. R. Thompson, and D. Mandrus, Phys. Rev. B **63**, 245113 (2001).
[15] S. Paschen, W. Carrillo-Cabrera, A. Bentien, V. H. Tran, M. Baenitz, Y. Grin, and F. Steglich, Phys. Rev. B **64**, 214404 (2001).
[16] A. Bentien, M. Christensen, J. D. Bryan, A. Sanchez, S. Paschen, F. Steglich, G. D. Stucky, and B. B. Iversen, Phys. Rev. B **69**, 045107 (2004).
[17] A. Bentien, S. Johnsen, and B. B. Iversen, Phys. Rev. B **73**, 094301 (2006).
[18] M. Christensen, A. B. Abrahamsen, N. B. Christensen, F. Juranyi, N. H. Andersen, K. Lefmann, J. Andreasson, C. R. H. Bahl, and B. B. Iversen, Nature Mater. **7**, 811 (2008).
[19] M. A. Avila, K. Suekuni, K. Umeo, H. Fukuoka, S. Yamanaka, and T. Takabatake, Appl. Phys. Lett. **92**, 041901 (2008).
[20] J. Martin, S. Erickson, G. S. Nolas, P. Alboni, T. M. Tritt, and J. Yang, J. Appl. Phys. **99**, 044903 (2006).
[21] N. L. Okamoto, K. Kishida, K. Tanaka, and H. Inui, J. Appl. Phys. **101**, 113525 (2007).
[22] X. Tang, P. Li, S. Deng, and Q. Zhang, J. Appl. Phys. **104**, 013706 (2008).
[23] S. Deng, X. Tang, P. Li, and Q. Zhang, J. Appl. Phys. **103**, 073503 (2008).
[24] A. Saramat, E. S. Toberer, A. F. May, and G. J. Snyder, J. Electron. Mater. **38**, 1423 (2009).
[25] C. Wood, D. Zoltan, and G. Stapfer, Rev. Sci. Instrum. **56**, 719 (1985).
[26] J. Martin, H. Wang, and G. S. Nolas, Appl. Phys. Lett. **92**, 222110 (2008).
[27] A. F. May, J.-P. Fleurial, and G. J. Snyder, Phys. Rev. B **78**, 125205 (2008).
[28] J. D. Bryan, N. P. Blake, H. Metiu, G. D. Stucky, B. B. Iversen, R. D. Poulsen, and A. Bentien, J. Appl. Phys. **92**, 7281 (2002).
[29] J. D. Bryan, V. I. Srdanov, G. D. Stucky, and D. Schmidt, Phys. Rev. B **60**, 3064 (1999).
[30] N. L. Okamoto, K. Kishida, K. Tanaka, and H. Inui, J. Appl. Phys. **100**, 073504 (2006).
[31] M. Christensen, N. Lock, J. Overgaard, and B. B. Iversen, J. Am. Chem. Soc. **128**, 15657 (2006).
[32] W. Carrillo-Cabrera, R. C. Gil, S. Paschen, Y. Grin, and Y. N. Hrin, Z. Kristallogr., New Cryst. Struct. **217**, 183 (2002).
[33] E. Alleno, G. Maillet, O. Rouleau, E. Leroy, and C. Godart, Chem. Mater. **21**, 1485 (2009).
[34] G. J. Miller, in *Chemistry, Structure, and Bonding of Zintl Phases and Ions* (VCH Publishers, New York, 1996).
[35] M. Christensen and B. B. Iversen, Chem. Mater. **19**, 4896 (2007).
[36] N. P. Blake, S. Latturner, J. D. Bryan, G. D. Stucky, and H. Metiu, J. Chem. Phys. **115**, 8060 (2001).
[37] G. K. H. Madsen, K. Schwarz, P. Blaha, and D. J. Singh, Phys. Rev. B **68**, 125212 (2003).
[38] V. I. Fistul, *Heavily Doped Semiconductors* (Plenum Press, New York, 1969).
[39] M. Hokazono, H. Anno, and K. Matsubara, Mater. Trans. **46**, 1485 (2005).
[40] N. L. Okamoto, T. Nakano, K. Tanaka, and H. Inui, J. Appl.

Phys. **104**, 013529 (2008).
[41] A. H. Wilson, *The Theory of Metals* (The Syndics of the Cambridge University Press, London, 1953).
[42] H. J. Goldsmid and J. W. Sharp, J. Electron. Mater. **28**, 869 (1999).
[43] J. R. Drabble and H. J. Goldsmid, *Thermal Conduction in Semiconductors* (Pergamon Press, New York, 1961).
[44] D. G. Cahill, S. K. Watson, and R. O. Pohl, Phys. Rev. B **46**, 6131 (1992).
[45] H. J. Goldsmid, *The Thermal Properties of Solids* (Dover Publications, Inc., New York, 1965).
[46] G. A. Slack and V. G. Tsoukala, J. Appl. Phys. **76**, 1665 (1994).
[47] G. J. Snyder and E. S. Toberer, Nature Mater. **7**, 105 (2008).
[48] G. S. Nolas (private communication).